

Passive Beam Shaping via Binary-Coded Apertures

Mohammed E. Eltayeb

Abstract—This paper presents coded-aperture reflector for indoor millimeter-wave (mmWave) coverage enhancement in obstructed or blocked line-of-sight (LoS) settings. We model the reflecting aperture using an equivalent array-factor formulation, where each passive reflecting cell contributes a reradiated field with phase set by the incident and departure directions. Building on this model, we develop two fabrication-friendly passive synthesis methods: (i) binary (1-bit) spatial coding that enables deterministic non-specular beam formation and multi-beam patterns by selecting cell participation on a dense lattice via an ON/OFF metallization mask, and (ii) diffraction-order (periodic) steering that exploits aperture periodicity to place selected diffraction orders at prescribed angles. We analytically characterize the proposed cosine-threshold quantization rule, including its asymptotic activation ratio and a distribution-free lower bound on non-specular gain relative to ideal continuous-phase control. To validate the proposed designs, we fabricate and metallize low-cost prototypes in-house using a copper-backed 3D-printed “inkwell” substrate with stencil-guided conductive-ink deposition. 60 GHz over-the-air measurements show non-specular gain enhancements on the order of +14–20 dB relative to passive, non-engineered (all-ON) reflector baselines. Results also demonstrate that fully passive, binary-coded apertures can deliver beam control with rapid in-lab manufacturability and offer a practical alternative to power-consuming reconfigurable surfaces for static indoor mmWave links.

Index Terms—Passive beamforming, binary aperture control, electromagnetic environment shaping, 3D-printed metasurfaces.

I. INTRODUCTION

Millimeter-wave (mmWave, 30–300 GHz) and terahertz (THz, 0.1–10 THz) bands enable multi-Gbps wireless links via wide contiguous bandwidths and support high-angular-resolution operation through highly directive apertures [1]–[3]. At the same time, short wavelengths intensify propagation challenges, including higher free-space loss, increased penetration loss through common building materials, and pronounced sensitivity to blockages and geometric shadowing [4], [5]. Consequently, practical indoor mmWave links often exhibit *persistent* coverage holes in obstructed-/blocked-LoS geometries such as corridor turns, non-specular corners, and junctions (e.g., L- and T-intersections), where even a strongly illuminated wall cannot deliver energy toward the user through mirror-like specular reflection. This motivates *electromagnetic environment shaping*, in which reflections are deliberately engineered to create reliable redirected paths that extend connectivity into non-line-of-sight (NLoS) regions without requiring additional active infrastructure.

A prominent environment-shaping approach is the reconfigurable intelligent surface or large intelligent surface (RIS

or LIS), which employs tunable unit cells (e.g., varactors, positive-intrinsic-negative (PIN) diodes, microelectromechanical systems (MEMS), or liquid crystals) to control the reflection coefficient across an aperture and redirect incident wavefronts [3], [6]–[9]. RIS can provide adaptivity, multi-user beam management, and programmable wavefront control, and has therefore received substantial attention in the communications and antennas communities. However, practical RIS deployments must contend with several non-idealities and overheads that are often overlooked in idealized phase-only models. First, finite-resolution phase tuning (quantization), mutual coupling, and element loss can reduce the realized array gain and distort sidelobe structure, especially at mmWave where fabrication tolerances and parasitics matter [8], [9]. Second, RIS operation typically relies on a control loop (CSI acquisition, optimization, and configuration), which can impose signaling overhead and latency, and can become challenging when the channel changes or when users are mobile [10]. Third, and central to the deployment perspective of this work, practical RIS require non-negligible DC power for controllers, driver/bias circuitry, and tunable elements, even if the RF scattering mechanism itself does not include a transmit chain [7], [11], [12]. Measurement-backed studies show that controller/driver power can be at the watt level and that unit-cell dissipation can be state dependent (e.g., for PIN-diode RIS, ON-state cells consume additional power) [11], [12]. For static indoor installations, these operational burdens translate into wiring complexity, power provisioning, maintenance considerations, and cost factors that matter in real deployments but are not captured by the usual “nearly-passive” narrative.

To reduce tuning and control complexity, recent work has explored quantized reconfigurable architectures [13]–[18]. Binary-phase RIS/metasurfaces using PIN diodes have been demonstrated at mmWave frequencies [13], and single-bit phase-shifter reflectarrays have been used for 60 GHz electronic steering [14]. Quantization artifacts such as grating/quantization lobes can be mitigated using additional structure (e.g., pseudo-random fixed delays combined with $0/\pi$ switching) [15]. While these platforms simplify phase control relative to multi-bit RIS, they still require bias networks, scalable routing/control, and continuous surface-side power whose overhead increases with aperture size [12], [18]. Thus, there remains a practical gap between (i) simple passive metallic reflectors that are robust and power-free but largely constrained to specular reflection, and (ii) fully programmable RIS that are flexible but impose nontrivial operational overhead.

This gap has renewed interest in *fully passive* reflectors for static or quasi-static deployments, where robustness, simplicity, and zero operational power are desirable. Prior studies show that simple passive reflectors (e.g., metallic panels) can enhance mmWave coverage in NLoS settings by creat-

This work was supported by the National Science Foundation under Grant No. NSF-2243089.

Mohammed E. Eltayeb is with the Department of Electrical and Electronic Engineering, California State University, Sacramento, USA. (Email: mohammed.eltayeb@csus.edu)

ing strong redirected paths when placed appropriately [19]–[22]. Beyond canonical plates, custom passive surfaces and application-specific passive designs have been explored to shape reflections more deliberately [23]–[25]. A representative example is *MilliMirror* [24], [25], which encodes a desired reflection phase profile through geometry (height) modulation of metal-backed dielectric structures. Geometry-coded phase panels can be highly effective, but they typically require a custom 3D thickness profile per beam pattern objective and can impose tighter tolerance requirements (e.g., printer z -resolution, warping/shrinkage, and material permittivity variation) when scaling to larger apertures.

A practical gap remains between simple passive reflectors, which are robust and power-free but largely limited to specular redirection, and reconfigurable surfaces, which provide flexible beam control at the cost of active hardware, control circuitry, and operational power. Geometry-coded passive reflectors offer another alternative, but they typically require a new 3-D design for each beam objective. To address this gap, this paper proposes a novel copper-backed 3D-printed inkwell reflector platform that combines a fixed dense scaffold with analytically derived binary metallization patterns. This structure enables rapid realization of different beam patterns on a common base reflector design, without requiring a new 3-D reflector geometry for each target response.

Within this framework, this work focuses on *binary-coded apertures* that generate deterministic non-specular beams using simple passive coding patterns. The reflecting aperture is modeled using an equivalent array-factor formulation, in which each passive reflecting cell contributes a reradiated field whose phase is determined by the incident and departure directions, as shown in Fig. 1. Building on this model, two fabrication-friendly passive synthesis methods are developed. First, a closed-form *cosine-threshold* rule is proposed to convert the ideal continuous phase ramp for one or more target directions into a fabrication-ready ON/OFF metallization mask on a dense $\lambda/2$ lattice. This *binary (1-bit) spatial coding* enables beam steering and multi-beam formation by selecting which cells participate in coherent addition. Second, *diffraction-order (periodic) steering* is developed by exploiting controlled aperture periodicity to place selected diffraction orders at prescribed angles. Both methods are strictly passive and require no bias network, tuning circuitry, or surface-side power.

The proposed coded apertures are best suited for quasi-static indoor settings where the geometry is known (or changes slowly) and where specular reflection alone does not illuminate the intended region. Representative cases include: (i) *L-corners and hallway turns* (including non-right-angle turns and gently curved corridors), where the dominant specular (mirror-angle) reflection fails to illuminate the region beyond the turn and coverage extension requires an engineered non-specular departure lobe toward the user; (ii) *T-intersections and corridor junctions*, where energy must be redirected into a side branch outside the specular footprint; and (iii) *doorway and room-corridor transitions*, where a panel near an opening must steer energy through the doorway to reach the interior. The approach is also useful in indoor multipath environments, where the propagation geometry supports multiple distinct reflected rays

from the same panel reaching the same user location. In such settings, a dominant specular component may be present but can be intermittently blocked or degraded by local destructive interference. By synthesizing one or more deterministic non-specular departure lobes, the reflector intentionally creates reflector-induced multipath to the same user. This improves robustness without reflector-side power requirement.

To validate the proposed theory-to-hardware pipeline, prototypes are fabricated using a copper-backed 3D-printed “inkwell” substrate with stencil-guided conductive-ink deposition. The reflector realization combines a fixed inkwell scaffold, an analytically derived binary ON/OFF mask pattern, and a stencil used to deposit conductive ink only into the selected wells. This enables rapid prototyping, since identical inkwell bases can be prepared in advance and metallized according to different mask patterns. Over-the-air (OTA) measurements at 60.48 GHz in single- and multi-beam configurations closely match the predicted steering behavior, confirming that fully passive binary-coded apertures can deliver deterministic non-specular beam formation with essentially zero operational power and deployment-friendly manufacturability.

The main contributions of this paper are summarized as follows

- We develop an array-factor model for binary-coded passive apertures and derive a closed-form cosine-threshold rule that maps an ideal phase profile to a fabrication-ready ON/OFF metallization mask.
- We analytically characterize the cosine-threshold mask, including its asymptotic activation ratio and a distribution-free lower bound on achievable non-specular target-lobe gain.
- We present a fully passive diffraction-order (periodic) design method and derive a closed-form period-selection rule to place a selected diffraction order at a prescribed departure angle.
- We show that deterministic non-specular beam formation is achievable without per-element geometry optimization by fabrication-coding patterns on a fixed dense lattice, in contrast to height-modulated reflectors (e.g., *MilliMirror* [24], [25]).
- We fabricate and metallize low-cost prototypes *in-house* using a copper-backed 3D-printed inkwell scaffold with stencil-guided conductive-paint deposition, enabling rapid iteration by swapping masks rather than reprinting a full 3D phase surface.
- We validate single- and multi-beam operation through 60.48 GHz over-the-air measurements, showing enhancements at intended non-specular directions consistent with theory for both mask-coded and diffraction-order designs.

Together, these contributions establish a low-complexity, fabrication-friendly framework for fully passive reflected-field control to enhance indoor NLoS coverage.

II. SYSTEM MODEL AND PROBLEM FORMULATION

A. System Model

We consider a narrowband mmWave link in which a transmitting node illuminates a planar, *fully passive* reflecting

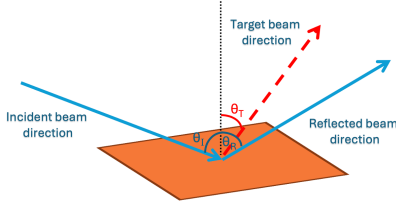


Fig. 1. Equivalent array-factor model for a passive reflecting element. Each passive element is modeled as an equivalent radiator whose far-field contribution carries the tangential phase associated with the incident and reradiated directions.

aperture that reradiates energy into the reflection half-space. The fabricated reflector used in this work is a 2-D lattice of candidate cells. Accordingly, we begin with a general 2-D planar aperture model, and then specialize it to the azimuth-plane case considered in this paper.

Let the reflector consist of $M_x \times M_y$ electrically reflecting cells located at

$$x_m = \left(\frac{M_x - 1}{2} - m \right) d_x, \quad m = 0, 1, \dots, M_x - 1, \quad (1)$$

$$y_n = \left(\frac{M_y - 1}{2} - n \right) d_y, \quad n = 0, 1, \dots, M_y - 1, \quad (2)$$

where d_x and d_y denote the lattice spacings along the two aperture axes. A dominant plane-wave component impinges on the reflector from direction (θ_I, ϕ_I) , where θ_I and ϕ_I denote the polar and azimuth angles, respectively, and the scattered field is observed toward direction (θ, ϕ) . Define the directional-cosine components

$$u(\theta, \phi) \triangleq \sin \theta \cos \phi, \quad v(\theta, \phi) \triangleq \sin \theta \sin \phi. \quad (3)$$

Under the standard far-field array-factor abstraction commonly used for RIS/reflectarrays [6], [7], [26], the complex baseband response can be written as

$$p(\theta, \phi; \theta_I, \phi_I) = \sum_{m=0}^{M_x-1} \sum_{n=0}^{M_y-1} \psi_{m,n} e^{-jk[x_m(u+u_I)+y_n(v+v_I)]}, \quad (4)$$

where $k = 2\pi/\lambda$, $\psi_{m,n}$ denotes the complex scattering coefficient of the (m, n) th cell, and

$$u = u(\theta, \phi), \quad v = v(\theta, \phi), \quad u_I = u(\theta_I, \phi_I), \quad v_I = v(\theta_I, \phi_I). \quad \theta \in \{\theta_{T,\ell}\}_{\ell=1}^L \Rightarrow |p(\theta, \theta_I)|^2 \text{ is maximized,}$$

$$\theta \notin \{\theta_{T,\ell}\}_{\ell=1}^L \Rightarrow |p(\theta, \theta_I)|^2 \text{ is minimized (or bounded).}$$

In this paper, we are primarily concerned with beam shaping in the azimuth plane. Accordingly, the azimuth angles are fixed to zero, i.e., $\phi = \phi_I = 0$. Under this restriction, (4) reduces to an azimuth-plane cut of the 2-D aperture response, namely

$$p(\theta, 0; \theta_I, 0) = \sum_{m=0}^{M_x-1} \sum_{n=0}^{M_y-1} \psi_{m,n} e^{-jkx_m(\sin \theta + \sin \theta_I)}. \quad (5)$$

Since the phase progression in (5) depends only on the x -coordinates, the 2-D response reduces to an equivalent one-dimensional (1-D) azimuthal model. For analytical tractability, we therefore adopt the 1-D formulation along the x -axis with M electrically reflecting cells (elements) located at

$$x_m = \left(\frac{M-1}{2} - m \right) d_0, \quad m = 0, 1, \dots, M-1, \quad (6)$$

where d_0 is the nominal lattice spacing. A dominant plane-wave component impinges on the reflector from the angle of arrival (AoA) θ_I (measured from aperture broadside), and the scattered field is observed toward an angle of departure (AoD) θ .

Under the same far-field array-factor abstraction, and omitting explicit zero-based indexing for clarity, the complex baseband response can be written in matrix form as

$$p(\theta, \theta_I) \triangleq \mathbf{a}^\top(\theta) \mathbf{\Psi} \mathbf{a}(\theta_I), \quad (7)$$

where $\mathbf{a}(\theta) \in \mathbb{C}^M$ is the 1-D steering vector

$$\mathbf{a}(\theta) \triangleq [e^{-jkx_0 \sin \theta}, e^{-jkx_1 \sin \theta}, \dots, e^{-jkx_{M-1} \sin \theta}]^\top, \quad (8)$$

and $\mathbf{\Psi} = \text{diag}(\psi_0, \dots, \psi_{M-1})$ captures the element-wise complex scattering coefficients. Expanding (7) yields the phasor summation

$$p(\theta, \theta_I) = \sum_{m=0}^{M-1} \psi_m e^{-jkx_m(\sin \theta + \sin \theta_I)}. \quad (9)$$

A uniform passive reflector corresponds to $\psi_m = 1$, which produces a dominant specular response at $\theta_{\text{spec}} = -\theta_I$.

B. Problem Formulation

This paper targets blocked-/obstructed-LoS indoor geometries in which extending coverage requires an engineered non-specular reflected path. In the most general 2-D setting, given incident direction (θ_I, ϕ_I) , the design objective is to choose a strictly passive aperture configuration that increases the response toward one or more desired departure directions $\{(\theta_{T,\ell}, \phi_{T,\ell})\}_{\ell=1}^L$. Equivalently, we seek passive design variables embedded in $\{\psi_{m,n}\}$ that shape the angular power pattern $|p(\theta, \phi; \theta_I, \phi_I)|^2$ to concentrate energy at the target direction(s).

In this paper, however, we focus on azimuth-plane beam shaping with $\phi_I = \phi = 0$. Under this restriction, the design problem reduces to choosing passive design variables embedded in $\{\psi_m\}$ that shape the azimuthal power pattern $|p(\theta, \theta_I)|^2$ to concentrate energy at one or more desired departure angles $\{\theta_{T,\ell}\}_{\ell=1}^L$. Using the scattering response in (9), we seek passive design parameters that shape the angular power pattern $|p(\theta, \theta_I)|^2$ such that

We pursue this goal using two complementary fully passive mechanisms:

1) *Fixed-aperture 1-bit ON/OFF spatial masking*: We realize beam shaping on a fixed dense lattice by selecting which cells participate in (9) using an ON/OFF metallization mask

$$\psi_m = b_m, \quad b_m \in \{0, 1\}. \quad (10)$$

Substituting (10) into (9) yields

$$p(\theta, \theta_I) = \sum_{m=0}^{M-1} b_m e^{-jkx_m(\sin \theta + \sin \theta_I)}, \quad (11)$$

where the binary sequence $\{b_m\}$ gates the element phasors and reshapes the spatial spectrum of the aperture.

2) *Diffraction-order (periodic) steering via uniform period selection*: As a second fully passive mechanism, we exploit aperture periodicity by enforcing a uniform effective inter-element period δ along the steering axis. Starting from the dense candidate lattice with spacing d_0 , we periodically activate elements so that adjacent active cells are separated by δ (typically $\delta = \kappa d_0 \geq d_0$ for some integer κ). For ideal passive elements ($\psi_m = 1$ on active sites), the periodicity produces discrete diffraction orders (grating lobes) whose angles are wavelength dependent. By choosing δ , a selected order can be aligned with a target AoD. This approach is attractive when aperture expansion is permissible, but becomes less suitable under fixed-footprint constraints.

C. Narrowband Assumption and Wideband Considerations

The analytical development in (9) assumes a narrowband model. Over wide bandwidths, the phase progression scales with $k(f) = 2\pi/\lambda(f)$, which can cause frequency-dependent beam pointing (beam squint) and target-direction gain variation when the physical reflector geometry (mask/period) is held fixed. Because the physical cell spacing is fixed, its electrical spacing varies with frequency; as frequency increases, the lattice becomes electrically sparser relative to the wavelength, whereas at lower frequencies it becomes electrically denser. This effect is typically more pronounced for diffraction-order designs because their lobe angles satisfy a wavelength-dependent grating condition. We quantify wideband behavior in Section VIII by sweeping frequency while keeping the physical design fixed.

III. PASSIVE BEAM SHAPING VIA FIXED-APERTURE 1-BIT SPATIAL MASK

This section develops a fully passive beam-shaping method based on a fixed-aperture 1-bit ON/OFF spatial mask implemented on a dense lattice. The reflector is fabrication-coded where each lattice location is either metallized (*ON*) and contributes a strong scattered field, or left unmetallized (*OFF*) and is suppressed. Under the array-factor abstraction, the ON/OFF pattern gates the phasor sum and reshapes the angular scattering response. The proposed synthesis strategy is as follows: (i) form the ideal continuous phase profile that yields coherent addition toward one or more desired departure directions, and (ii) map that profile to a fabrication-friendly binary mask using a closed-form cosine-threshold rule.

A. Binary Mask Model

Consider a 1-D aperture with M candidate locations along the x -axis, spaced by d_0 at positions x_m in (6). Let $b_m \in \{0, 1\}$ denote the state of the m th location, where $b_m = 1$ corresponds to an ON (reflecting) cell and $b_m = 0$ corresponds to an OFF (suppressed) cell. Define the diagonal mask matrix

$$\mathbf{B} \triangleq \text{diag}(b_0, b_1, \dots, b_{M-1}). \quad (12)$$

For an incident plane wave arriving from AoA θ_I , the complex response observed toward AoD θ is

$$p(\theta, \theta_I) = \mathbf{a}^\top(\theta) \mathbf{B} \mathbf{a}(\theta_I) = \sum_{m=0}^{M-1} b_m e^{-jkx_m(\sin\theta + \sin\theta_I)}, \quad (13)$$

which is the specialization of (7) with $[\Psi]_{m,m} = b_m$. Equation (13) shows that the binary mask $\{b_m\}$ gates the element phasors where ON cells participate in coherent addition and OFF cells are removed from the sum.

In practice, reflection imperfections and ohmic/dielectric loss can be captured by replacing the ON state with an amplitude coefficient $b_m = \rho$ (with $0 < \rho \leq 1$), while retaining $b_m = 0$ for the OFF state. For ease of exposition, this paper assumes $b_m \in \{0, 1\}$ and does not explicitly model such non-ideal reflection amplitudes.

B. Closed-Form 1-Bit Mask Construction

We now derive a closed-form ON/OFF mask that steers energy toward a desired target AoD θ_T (or multiple targets) under incidence θ_I .

1) *Ideal continuous phase profile*: To phase-align all active contributions toward θ_T , an ideal programmable reflector would apply the compensating phase

$$\phi_m \triangleq kx_m(\sin\theta_T + \sin\theta_I), \quad (14)$$

so that the terms in (13) add constructively at $\theta = \theta_T$.

2) *Cosine-threshold ON/OFF mapping*: We first quantize the ideal unit-modulus phasor $e^{j\phi_m}$ onto the bipolar alphabet $\{+1, -1\}$ via nearest-neighbor projection as follows (see Fig. 2)

$$\begin{aligned} \hat{w}_m &= \arg \min_{w \in \{+1, -1\}} |e^{j\phi_m} - w|^2 = \text{sgn}(\Re\{e^{j\phi_m}\}) \\ &= \text{sgn}(\cos \phi_m) \in \{+1, -1\}. \end{aligned} \quad (15)$$

The bipolar alphabet corresponds to a 1-bit $0/\pi$ reflection-phase surface. Realizing $\hat{w}_m = -1$ in passive hardware requires a reflection phase shift of approximately π with comparable magnitude, which cannot be obtained by metallization presence/absence alone. Achieving a true -1 state therefore requires an additional passive modulation mechanism (e.g., geometry-encoded phase such as thickness/height modulation over a ground plane), which is outside the scope of the fabrication approach used here.

Since the fabricated surface in this work realizes a binary amplitude state, we map the bipolar code to an ON/OFF mask by assigning $+1 \mapsto 1$ (ON) and $-1 \mapsto 0$ (OFF) as follows

$$b_m \triangleq \frac{\hat{w}_m + 1}{2} \iff b_m = \mathbf{1}\{\cos \phi_m \geq 0\}, \quad (16)$$

where $\mathbf{1}\{\cdot\}$ denotes the indicator function, i.e., $\mathbf{1}\{\mathcal{A}\} = 1$ if the condition \mathcal{A} is true and $\mathbf{1}\{\mathcal{A}\} = 0$ otherwise. Thus, the mask retains locations whose ideal phases lie in the constructive half-plane and suppresses those that would contribute destructively at θ_T .

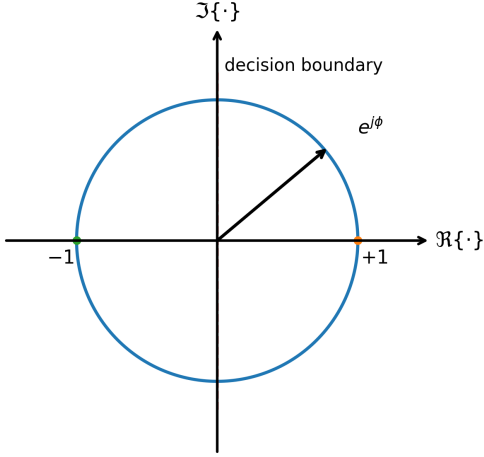


Fig. 2. Geometric view of 1-bit phase quantization on the unit circle. The ideal phasor $e^{j\phi}$ is mapped to $\{+1, -1\}$ using the sign of $\Re\{e^{j\phi}\} = \cos\phi$. The fabricated reflector implements the associated ON/OFF mask via metallization (ON) or suppression (OFF).

3) *Extension to multiple target directions:* For L target AoDs $\{\theta_{T,\ell}\}_{\ell=1}^L$ with complex weights $\{\alpha_\ell\}$, we superpose the ideal phase ramps and threshold the real part to obtain

$$s_m \triangleq \sum_{\ell=1}^L \alpha_\ell \exp(jk(\sin\theta_{T,\ell} + \sin\theta_I)x_m), \quad (17)$$

$$b_m \triangleq \mathbf{1}\{\Re\{s_m\} \geq 0\}. \quad (18)$$

This produces a single binary pattern that can create multiple deterministic non-specular lobes.

4) *Global phase offset for finite-aperture robustness:* For finite M , the thresholding in (16) can be sensitive to how the discrete samples fall relative to the decision boundary $\cos(\phi_m) = 0$. We therefore allow a constant phase offset ψ prior to thresholding as follows

$$b_m(\psi) \triangleq \mathbf{1}\{\cos(\phi_m + \psi) \geq 0\}. \quad (19)$$

The offset does not change the phase-ramp slope (hence does not change the target geometry), but it can improve finite-aperture performance by shifting the threshold relative to the sample phases. Unless otherwise stated, we set $\psi = 0$ in this paper.

C. Thinning Ratio (ON Fraction)

A direct consequence of ON/OFF masking is aperture thinning. Define the ON fraction (thinning ratio)

$$\eta_M \triangleq \frac{1}{M} \sum_{m=0}^{M-1} b_m. \quad (20)$$

Lemma 1 (Asymptotic 50% thinning ratio for the single-target cosine-threshold mask): Consider $b_m = \mathbf{1}\{\cos(\phi_m) \geq 0\}$ with phase progression $\phi_{m+1} - \phi_m = kd_0(\sin\theta_T + \sin\theta_I)$. If

$$\frac{kd_0(\sin\theta_T + \sin\theta_I)}{\pi} \notin \mathbb{Q}, \quad (21)$$

then

$$\lim_{M \rightarrow \infty} \eta_M = \frac{1}{2}. \quad (22)$$

Proof: See Appendix A.

Lemma 1 shows that the cosine-threshold construction activates asymptotically half of the available locations for generic steering geometries. Condition (21) excludes only degenerate cases where the phase increment is exactly commensurate with the π -periodic sign structure of the cosine threshold. Fig. 3(a) illustrates Lemma 1 by showing that the ON fraction (thinning ratio) η_M converges toward 0.5 as the number of elements increases for a representative steering geometry.

D. Distribution-Free Target-Lobe Gain Bound

We next quantify the achievable target-direction gain at $\theta = \theta_T$. Define the coherent sum toward the target as

$$S_M(\mathbf{b}) \triangleq \sum_{m=0}^{M-1} b_m e^{-j\phi_m}, \quad S_M^* \triangleq \max_{\mathbf{b} \in \{0,1\}^M} |S_M(\mathbf{b})|, \quad (23)$$

and the normalized target-lobe gain as

$$\gamma \triangleq \frac{|S_M(\mathbf{b})|^2}{M^2}, \quad \gamma^* \triangleq \max_{\mathbf{b} \in \{0,1\}^M} \gamma = \frac{(S_M^*)^2}{M^2}. \quad (24)$$

Lemma 2 establishes a distribution-free lower bound on the best achievable normalized target-lobe gain under the ON/OFF masking constraint.

Lemma 2 (Distribution-free gain bound for single-target ON/OFF masking): For arbitrary element locations $\{x_m\}$ and any incidence/target angles (θ_I, θ_T) , the maximum achievable normalized target-lobe gain satisfies

$$\gamma^* \geq \frac{1}{\pi^2}. \quad (25)$$

Proof: See Appendix B.

Lemma 2 gives a worst-case guarantee on target-direction performance under the ON/OFF masking constraint. Specifically, the maximum normalized target-lobe gain is always at least $1/\pi^2$, which corresponds to a worst-case loss of 9.94 dB relative to the ideal continuous-phase upper bound. Fig. 3(b) illustrates this result by comparing the normalized target-lobe gain of ON/OFF masking with bipolar (± 1) and ideal continuous-phase control. As expected, ± 1 control incurs a smaller loss (about 3.9 dB), since sign reversals can re-phase contributions that ON/OFF masking must suppress; a similar 3.9 dB 1-bit quantization loss was reported in [29], though this work uses a closed-form 1-bit assignment rule. The figure also confirms the 9.94 dB worst-case ON/OFF loss established by Lemma 2. Finally, at $\sin\theta_T + \sin\theta_I = 0$, all schemes achieve $\gamma = 1$ (0 dB), corresponding to the specular-reflection condition.

IV. DIFFRACTION-ORDER (GRATING-LOBE) BEAM STEERING VIA UNIFORM PERIOD SELECTION

Section III introduced fixed-aperture ON/OFF masking on a dense $d_0 \approx \lambda/2$ scaffold. Here we present a complementary passive mechanism based on uniform-period activation. The key design parameter is the inter-element spacing (period)

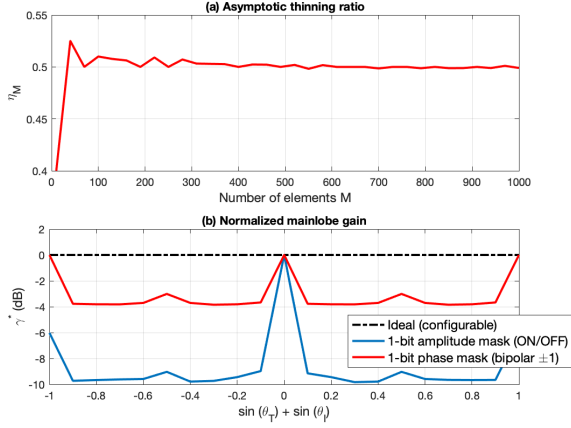


Fig. 3. (a) Thinning ratio η_M versus number of elements for $\theta_I = 60^\circ$ and $\theta_T = -30^\circ$, illustrating convergence to 0.5 (Lemma 1). (b) Normalized target-lobe gain $\gamma = |S_M|^2/M^2$ versus $\sin \theta_T + \sin \theta_I$ for $M = 64$ and $d/\lambda = 0.5$. ON/OFF masking incurs a worst-case loss of 9.94 dB relative to ideal continuous-phase control and ≈ 6 dB relative to ± 1 control, consistent with Lemma 2.

δ between adjacent active reflecting elements, with $\delta \geq d_0$. In practice, δ can be realized by activating elements with a periodic pattern on the dense lattice (e.g., activating every m th lattice location along the synthesis dimension so that $\delta = \kappa d_0$). A uniformly periodic aperture produces a discrete set of reflected lobes indexed by an integer diffraction order n . By selecting (δ, n) , a chosen order (grating lobe) can be placed at a desired target departure angle using closed-form relationships.

A. Uniform-Period Array-Factor Model

Consider a linear reflector of M identical reflecting elements with uniform inter-element spacing δ (distance between adjacent active elements). Using the centered indexing in (6), the element coordinates are

$$x_m \triangleq \left(\frac{M-1}{2} - m \right) \delta, \quad m = 0, 1, \dots, M-1. \quad (26)$$

A plane wave impinges from AoA θ_I and the scattered field is observed toward AoD θ_T in the reflection half-space. Generalizing (9) to uniform weights ($[\Psi]_{m,m} = 1$) gives

$$p(\theta_T, \theta_I) = \sum_{m=0}^{M-1} e^{-j k x_m (\sin \theta_T + \sin \theta_I)}. \quad (27)$$

B. Diffraction Orders and Single-Beam Steering

For a uniformly periodic aperture, (27) admits the closed form [26]

$$p(\theta_T, \theta_I) = e^{-j \frac{(M-1)}{2} \delta (k_I + k_T)} \frac{\sin\left(\frac{M}{2} \delta (k_I + k_T)\right)}{\sin\left(\frac{1}{2} \delta (k_I + k_T)\right)}, \quad (28)$$

where $k_I \triangleq k \sin \theta_I$ and $k_T \triangleq k \sin \theta_T$. The principal maxima occur when the inter-element phase increment is an integer multiple of 2π , i.e. $\frac{\delta}{\lambda} (\sin \theta_I + \sin \theta_T) = n, n \in \mathbb{Z}$. Each

integer n defines a diffraction order (a candidate reflected lobe). The departure angle of order n can be written as

$$\theta_n = \sin^{-1} \left(n \frac{\lambda}{\delta} - \sin \theta_I \right). \quad (29)$$

1) *Closed-form period for steering to a target AoD:* To align order n with a desired AoD θ_T , enforce $\theta_n = \theta_T$ in (29) to obtain

$$\delta^*(n) = \frac{n\lambda}{\sin \theta_T + \sin \theta_I}. \quad (30)$$

For single-beam steering, we set $n = \pm 1$ to minimize the distance. For $n = 1$,

$$\delta^* = \frac{\lambda}{\sin \theta_T + \sin \theta_I}. \quad (31)$$

C. Multi-Beam Operation via Multiple Visible Diffraction Orders

Multiple diffraction orders may be visible in the far field. Order n is visible only if the argument of $\sin^{-1}(\cdot)$ in (29) lies in $[-1, 1]$, and hence

$$\left| n \frac{\lambda}{\delta} - \sin \theta_I \right| \leq 1. \quad (32)$$

The corresponding integer range of visible orders becomes

$$n_{\min} = \left\lceil \frac{\delta}{\lambda} (\sin \theta_I - 1) \right\rceil, \quad n_{\max} = \left\lfloor \frac{\delta}{\lambda} (\sin \theta_I + 1) \right\rfloor, \quad (33)$$

with $N_{\text{orders}} = n_{\max} - n_{\min} + 1$. If a second target AoD coincides with one of the visible θ_n , the same δ illuminates it; otherwise, δ and/or the chosen order can be redesigned subject to physical constraints.

V. 3D-PRINTED “INKWELL” PROTOTYPES AND STENCIL-BASED FABRICATION

This section describes the low-cost fabrication workflow used to realize and experimentally validate the two fully passive beam-shaping mechanisms developed in this paper, namely (i) fixed-aperture 1-bit spatial masking (Section III) and (ii) diffraction-order (uniform-period) steering (Section IV). Both designs are implemented on a common 3D-printed “inkwell” reflector platform, in which a planar aperture is discretized into a dense lattice of candidate metallization locations. The reflector realization involves three components. The first is the 3D-printed inkwell scaffold, which serves as the physical base platform. The second is the analytically derived binary mask pattern, which specifies the ON/OFF metallization layout. The third is the stencil, which is used during fabrication to deposit conductive ink only into the selected wells. Since the beam synthesis in this paper is carried out for azimuthal steering with the elevation angle fixed to zero, the fabricated prototypes are realized on a 2-D lattice by replicating the same 1-D azimuthal pattern across rows. The reflector dimensions, lattice parameters, material choices, and operating frequency used in this paper are summarized in Table I.

Fig. 4 shows a representative reflector cell in top and side view. Each cell consists of a conductive ink/metallized fill inside an inkwell cavity, a 3D-printed dielectric scaffold, and

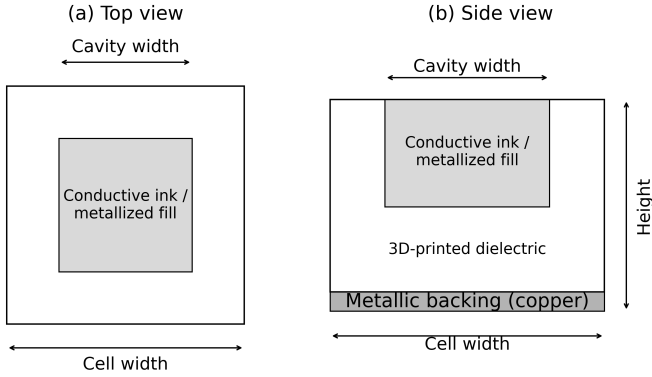


Fig. 4. Representative reflector cell (element) geometry: (a) top view and (b) side view. The cell consists of a conductive ink/metallized fill formed inside the inkwell cavity, a 3D-printed dielectric scaffold, and a metallic copper backing in direct contact with the dielectric.

a metallic copper backing realized using copper adhesive tape directly attached to the dielectric. This yields a metal-backed dielectric structure similar in structural spirit to prior passive reflector implementations such as MilliMirror [24], although the present work does not rely on thickness-tuned unit-cell phase synthesis.

The fabricated reflectors are designed using the aperture-level analytical array model developed in this paper. In this model, each lattice location is treated as an effective reflector sample contributing to the reradiated field. The active (metallized) locations are selected either by the cosine-threshold rule described in Section III-B or by the periodic-spacing selection described in Section IV-A. These analytical results are used both to design the fabricated reflectors and to generate the corresponding theoretical patterns. Accordingly, this work does not include full-wave extraction of element-level reflection magnitude and phase under normal or oblique incidence, as would be done in a Computer Simulation Technology (CST) or High Frequency Structure Simulator (HFSS)-based metasurface unit-cell analysis. Similar element-/surface-level abstractions are also common in RIS system modeling [6], [7]. In the analytical model, metallized cells are treated as ideal reflecting points, while non-metallized cells are assumed to contribute negligibly to the reflected field. Full-wave element-level reflection characterization under normal and oblique incidence is left for future work.

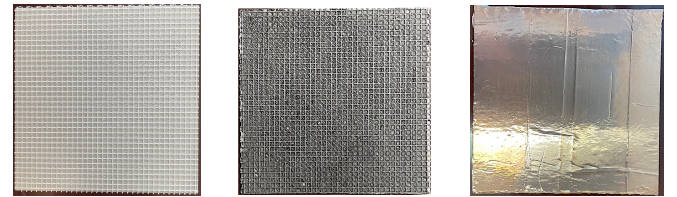
A. Common “Inkwell” Geometry and Relation to the Array Model

Fig. 5(a) shows the bare 3D-printed inkwell base used in this paper. The aperture is discretized into a uniform candidate lattice with pitch $d_0 = 2.5$ mm. Each candidate location is a square inkwell with a 2.2×2.2 mm opening and depth ≈ 0.4 mm, printed into a dielectric base of total thickness ≈ 0.8 mm (approximately 0.4 mm bottom floor plus 0.4 mm wall layer). The well walls (i) confine conductive ink during deposition and (ii) enforce a repeatable metallized footprint across prototypes.

From a modeling perspective, the inkwell grid provides a fixed sampling scaffold for implementing the diagonal aperture

TABLE I
GEOMETRY, MATERIAL, AND FABRICATION PARAMETERS OF THE 3D-PRINTED “INKWELL” REFLECTOR PLATFORM USED IN THIS PAPER.

Parameter	Value / Description
Aperture size	90×90 mm (square), centered at (0, 0)
Candidate grid (scaffold)	35×35 wells (1225 locations)
Center-to-center pitch	$d_0 = 2.5$ mm in x and y ($\approx \lambda/2$ at 60.48 GHz)
Inkwell opening (front)	2.2×2.2 mm square
Inkwell depth	≈ 0.4 mm (ink reservoir)
Base thickness	≈ 0.8 mm total (~ 0.4 mm bottom dielectric floor + ~ 0.4 mm wall layer)
Stencil thickness	≈ 0.8 mm
Stencil aperture	2.1×2.1 mm square (slightly smaller than wells)
Substrate material	3D-printed dielectric (PLA/PETG)
Metallization	SilexCore conductive paint [27] deposited into wells (stencil-guided for masks)
Ground plane	Continuous copper tape/sheet on rear face (high reflectivity at 60.48 GHz)



(a) Bare inkwell base. (b) All-ON front. (c) All-ON back. copper-backed rear.

Fig. 5. All-ON reference reflector: (a) bare base, (b) metallized front, (c) copper-backed rear.

interaction Ψ in the array-factor model. For spatial masking, a subset of wells is metallized to realize $b_m \in \{0, 1\}$, thereby implementing the binary aperture described in Section III. For diffraction-order steering, entire columns are metallized with a uniform effective spacing δ to implement the periodic aperture described in Section IV. Metallization is implemented by filling selected inkwells with a commercial water-based conductive paint [27]. Fig. 5(b) shows the resulting all-ON configuration, where all wells are metallized. Since this paper targets azimuthal beam shaping, the designed 1-D pattern along the x -axis is replicated across the y -axis (constant vertical pitch), producing a striped 2-D aperture.

B. Copper-Foil Backing as a Passive Ground Plane

All prototypes use a continuous copper-foil tape layer on the rear side of the printed base to form a conductive ground plane (Fig. 5(c)). This backing is critical at 60 GHz as it provides a high-conductivity termination that increases reflection efficiency and ensures that the front-side pattern (modulated by ON/OFF metallization or periodic activation) perturbs a strong reflected field.

C. Stencil Layer for Repeatable Binary Metallization

For spatial-masking prototypes, we fabricate a matching 3D-printed stencil that enforces the designed ON/OFF pat-

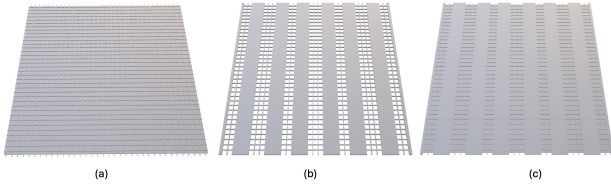


Fig. 6. Inkwell base and matching stencil (CAD/STL views). (a) Base with all wells present. (b) Stencil used to metallize selected wells (ON locations). (c) Optional “matched-base” variant in which OFF locations are removed in the print; in this work, we use the base matched to the stencil (c)+ stencil(b), but either (a)+(b) or (c)+(b) can be used.

tern during conductive-ink deposition. The stencil (thickness ≈ 0.8 mm) contains square openings of 2.1×2.1 mm (slightly smaller than the 2.2×2.2 mm well openings) to reduce edge bleeding and improve pattern fidelity. The stencil is closed everywhere except at intended ON locations so that the designed binary sequence is mapped into a repeatable metallization pattern. Fig. 6 shows representative computer-aided design (CAD) and stereolithography (STL) renderings of the inkwell base and a corresponding stencil for a $(\theta_I, \theta_T) = (30^\circ, -60^\circ)$ design case.

D. Prototype Classes and Fabrication Workflow

Using the common printing-and-deposition workflow, we fabricate three prototype classes which correspond to the designs analyzed in Sections III and IV. Each prototype is realized by (i) 3D-printing the inkwell base (and a matching stencil), (ii) applying a continuous copper ground plane to the rear face, and (iii) depositing conductive paint into the selected inkwells. For mask-coded designs, the stencil confines deposition to the intended ON locations to improve pattern fidelity and repeatability.

The all-ON reference reflector in Fig. 5(b) metallizes all 35×35 wells and serves as a baseline specular/reference response for measurement validation. For fixed-aperture 1-bit spatial masking, the distance remains fixed at $d_0 = 2.5$ mm and beam control is achieved by metallizing a subset of wells according to the designed binary mask. For diffraction-order steering, beam (lobe) placement is achieved by metallizing columns with a uniform effective spacing δ , with each active column replicated across rows to form a periodic 2-D pattern.

Fig. 7 shows fabricated prototypes for two representative steering configurations, $(\theta_I, \theta_T) = (30^\circ, -60^\circ)$ and $(\theta_I, \theta_T) = (45^\circ, -10^\circ)$, comparing spatial-mask and diffraction-order realizations on the same inkwell platform. These prototypes are used in Section VIII to validate the proposed beam-control methods through 60.48 GHz azimuthal sweeps.

VI. PERFORMANCE CRITERIA AND EVALUATION METRICS

This section defines the metrics used to evaluate the fully passive, fabrication-coded reflectors. The proposed apertures are designed to synthesize deterministic non-specular departure lobes toward intended user directions. We quantify (i) target-direction power delivery and (ii) system-level impact under reflector-side operational-power constraints.

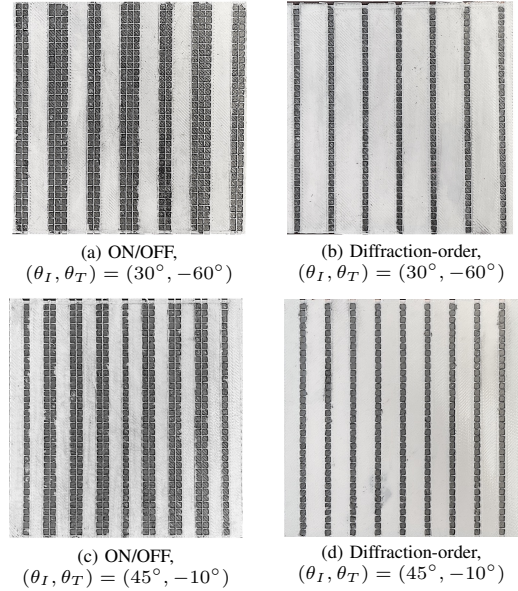


Fig. 7. Fabricated prototypes on the inkwell substrate (ON/OFF mask vs. diffraction-order).

VII. PERFORMANCE CRITERIA AND EVALUATION METRICS

This section defines the metrics used to evaluate the fully passive, fabrication-coded reflectors developed in this paper. The proposed apertures are designed to generate deterministic non-specular departure lobes toward intended user directions. Their performance is quantified in terms of (i) target-direction response and (ii) system-level impact under reflector-side operational-power constraints.

A. Angular Pattern Metrics

For a fixed incidence angle θ_I , the theoretical angular power pattern is defined as

$$P(\theta; \theta_I) \triangleq |p(\theta, \theta_I)|^2, \quad (34)$$

where θ denotes the departure angle in the reflection half-space. For the 1-D model with M elements, we define the normalized gain as follows

$$\gamma(\theta; \theta_I) \triangleq \frac{P(\theta; \theta_I)}{M^2}, \quad (35)$$

and for a desired target departure angle θ_T , the target-direction power is

$$G_T \triangleq P(\theta_T; \theta_I). \quad (36)$$

B. System-Level Mapping and Energy Efficiency

To connect target-direction performance to a system-level metric, we map the target-direction signal-to-noise ratio (SNR) to an achievable rate using the Shannon formula

$$R(\theta_T) \triangleq B \log_2(1 + \text{SNR}(\theta_T)), \quad (37)$$

where B is the communication bandwidth. In the theoretical comparisons, $\text{SNR}(\theta_T)$ can be interpreted as scaling with the

target-direction gain G_T in (36). Energy efficiency is then computed as [11], [12], [28]

$$\text{EE} \triangleq \frac{R(\theta_T)}{P_{\text{TX}} + P_{\text{circ}} + P_{\text{surf}}}, \quad (38)$$

where P_{TX} is the radiated transmit power, P_{circ} is the fixed radio/baseband power excluding P_{TX} , and P_{surf} is the surface-side operational power required by the reflecting structure. Energy efficiency is a key deployment metric because it captures delivered throughput per unit total power and explicitly accounts for surface-side overhead that impacts long-term operation in static installations. Combining (37) and (38) yields

$$\text{EE}(\theta_T) = \frac{B \log_2(1 + \text{SNR}(\theta_T))}{P_{\text{TX}} + P_{\text{circ}} + P_{\text{surf}}},$$

which shows that EE increases with target-direction SNR through $R(\theta_T)$ and decreases with total power consumption, particularly the surface-side overhead P_{surf} in powered RIS architectures. For the proposed passive designs, no biasing or control circuitry is required after installation, and thus $P_{\text{surf}} \approx 0$ during operation.

VIII. RESULTS AND DISCUSSION

This section presents both theoretical and experimental results for the proposed fully passive coded reflectors. Section VIII-A analyzes the performance of 1-bit ON/OFF masking and diffraction-order steering using the proposed aperture-level models. Section VIII-B then reports over the air measurements and discusses their agreement with theory, along with implications for practical deployment.

The 1-D array-factor expression in (9) is used to generate the azimuth-plane plots, whereas the planar-aperture model in (4) is used to generate the corresponding 2-D angular maps and 3-D patterns. For the ON/OFF design, the ideal target-direction phase profile is first formed using (14), then converted to a binary mask using the cosine-threshold rule in (16), and finally evaluated in the array model. The resulting binary vector \mathbf{b} directly determines the metallized cell locations in the fabricated reflector, i.e., entries with $b_m = 1$ identify the wells that are filled with conductive ink, while entries with $b_m = 0$ remain unmetallized. Thus, the same analytically derived mask is used both to generate the theoretical ON/OFF plots and to define the metallization pattern of the 3D-printed prototype.

For the diffraction-order design, the required period is first obtained from the closed-form design rule in (31), and the resulting angular response is then computed using the uniform-period model in (27). That analytically determined period is also used to set the spacing of the active metallized columns in the fabricated 3D-printed diffraction-order prototype. In the 2-D evaluations, the same 1-D azimuthal design is replicated across rows to form the corresponding 2-D coded aperture. Accordingly, all theoretical plots reported in this section are analytical evaluations of the proposed aperture-level models, and the same analytical design parameters are used to define the physical metallization pattern and spacing of the fabricated prototypes.

To position the proposed approach relative to closely related designs, several benchmark cases are used throughout the

theoretical and experimental evaluation. In the theoretical results, the proposed ON/OFF reflector is compared against three reference designs: a 1-bit (± 1) benchmark motivated by discrete-state RIS literature [29], a conventional all-ON passive reflector baseline representing non-engineered specular reflection as in prior passive mmWave reflector studies [19], and an ideal continuous-phase reflector serving as an upper-bound reference for target-direction gain, consistent with common RIS/LIS benchmarking practice [6], [7]. In the experimental results, the fabricated designs are compared against both the passive all-ON reflector and a smooth copper plate of the same aperture size. The copper plate serves as a conductor reference to verify that the all-ON metallized inkwell reflector exhibits comparable specular behavior. These benchmarks help clarify that the contribution of this work is a fully passive, fabrication-friendly coded-aperture reflector framework that enables target-direction beam shaping without requiring active tuning circuitry or a new 3-D geometry redesign for each beam objective.

A. Theoretical Results

Unless otherwise stated, all theoretical results and figures in this section are obtained by evaluating the proposed analytical aperture-level models in MATLAB. No full-wave unit-cell simulations are used in this work. The ON/OFF results are generated using the formulation in Section III, whereas the diffraction-order results are generated using the periodic steering formulation in Section IV. Unless otherwise stated, the analysis is carried out at 60 GHz using $M = 35$ and $d_0/\lambda = 0.5$.

1) *Single-target synthesis*: $\theta_I = 45^\circ$, $\theta_T = -10^\circ$: Fig. 8 compares the normalized gain $\gamma(\theta; \theta_I)$ for four reflector configurations: the conventional all-ON passive aperture, the proposed ON/OFF mask, a bipolar (± 1) 1-bit reflector included as a discrete-state benchmark [29], and an ideal continuous-phase reflector included as an upper-bound reference [6], [7]. The all-ON aperture exhibits the expected specular-dominated response, with its strongest lobe at $\theta_{\text{spec}} = -\theta_I = -45^\circ$ and only weak non-specular reflection. By contrast, the proposed ON/OFF mask produces a deterministic non-specular lobe toward $\theta_T = -10^\circ$ by activating a subset of lattice locations according to the cosine-threshold rule.

The non-specular target response of ON/OFF masking exhibits a 9.94 dB loss relative to the ideal continuous-phase upper bound. This is consistent with Lemma 2, which lower-bounds the maximum achievable normalized target-lobe gain by $1/\pi^2$ (i.e., $10 \log_{10}(1/\pi^2) = -9.94$ dB). This loss is fundamentally due to amplitude-only control where an ideal surface can phase-align all M contributions at the target. ON/OFF masking can only retain or suppress elements and cannot re-phase unfavorable contributions. At the specular direction, the ON/OFF pattern incurs a smaller loss (approximately 6.9 dB) because the all-ON aperture is already phase-aligned and applying a non-specular mask primarily reduces the effective aperture through thinning and redistributes energy into other angles. In particular, Lemma 1 shows an asymptotic activation ratio near 50%, contributing an order-of-3 dB reduction, with the remaining loss attributable to the

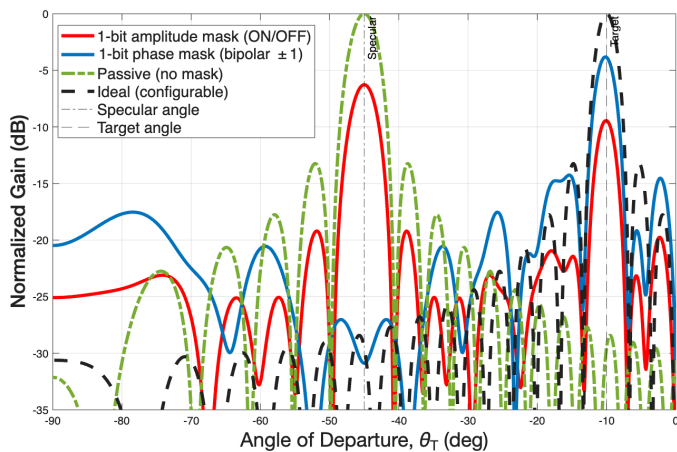


Fig. 8. Theory (60 GHz, $\theta_I = 45^\circ$, target $\theta_T = -10^\circ$, $M = 35$, $d_0/\lambda = 0.5$). Normalized gain $\gamma(\theta; \theta_I)$ for all-ON, 1-bit ON/OFF (cosine-threshold), 1-bit bipolar (± 1) (cosine-threshold), and an ideal continuous-phase reflector.

non-uniform spatial weighting introduced to form the non-specular lobe. The bipolar (± 1) mask allows sign reversals and therefore more closely approximates the ideal coherent sum at the target, yielding an ≈ 3.9 dB loss, consistent with 1-bit phase quantization trends reported in [29].

2) Diffraction-order steering (unconstrained aperture):

Diffraction-order steering forms a non-specular lobe by enforcing a uniform effective period δ so that a chosen diffraction order satisfies the grating condition for the desired departure angle θ_T (Section IV). Fig. 9 illustrates $(\theta_I, \theta_T) = (45^\circ, -10^\circ)$ at 60 GHz with $\delta = 9.37$ mm, where all $M = 35$ elements are active on the periodic lattice. With this choice of δ , a strong diffraction order is placed at $\theta_T = -10^\circ$ while the zeroth-order (specular) response at $\theta_{\text{spec}} = -45^\circ$ is retained, as expected for a uniform-amplitude periodic aperture.

Because all elements participate coherently for the selected order, the target-lobe peak can approach the ideal continuous-phase upper bound in the unconstrained-aperture setting shown in Fig. 9. This gain advantage, however, is achieved by increasing the inter-element spacing from the dense scaffold spacing ($d_0 = 2.5$ mm $\approx \lambda/2$) to $\delta = 9.37$ mm, which expands the physical aperture when M is held fixed. The increased aperture length leads to narrower angular features (sharper main lobes and nulls) which can make alignment more sensitive in practice.

3) Multi-target synthesis: $\theta_I = 30^\circ$, $\theta_T \in \{-7.8^\circ, -60^\circ\}$:

Fig. 10 considers a two-target design obtained by complex superposition of the desired phase ramps followed by binary thresholding as in (17)–(18). The ON/OFF mask produces two deterministic non-specular lobes at $\theta_T = -7.8^\circ$ and -60° while retaining a residual specular component at $\theta_{\text{spec}} = -30^\circ$, which is expected under amplitude-only control. The bipolar (± 1) mask, by allowing sign reversals, more closely tracks the ideal continuous-phase reference and yields higher per-target coherence.

In the ideal continuous-phase case, the reflected energy is intentionally split across two directions, and therefore the peak gain at each target is reduced relative to the single-target setting. The ON/OFF and bipolar curves exhibit the same

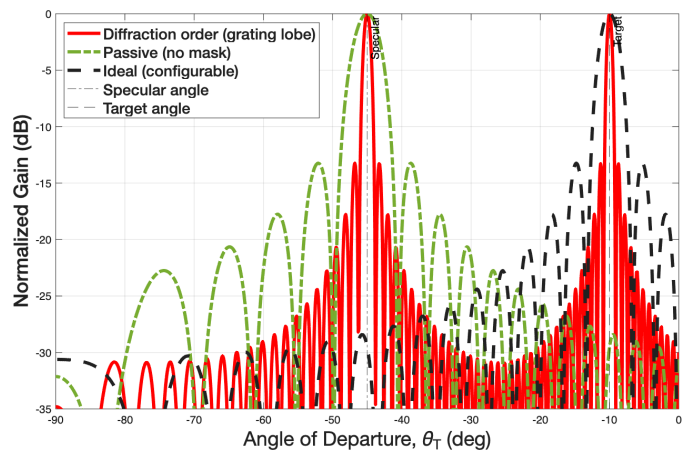


Fig. 9. Theory (60 GHz, $\theta_I = 45^\circ$, target $\theta_T = -10^\circ$, $M = 35$). Diffraction-order steering with period $\delta = 9.37$ mm (all-ON), producing a grating lobe at θ_T while retaining the zeroth-order (specular) lobe.

trend, with per-target peaks reduced by power sharing and by the 1-bit constraint. Notably, the characteristic loss behavior observed in the single-target case is preserved. When compared to the ideal continuous-phase reference, the ON/OFF masking exhibits ≈ 10 dB non-specular penalty relative to ideal continuous-phase control, while the specular component experiences a lower reduction due to thinning and energy redistribution (as discussed for Fig. 8).

Fig. 11 shows a diffraction-order multi-lobe example where a larger effective period ($\delta = 13.66$ mm) produces multiple visible diffraction orders alongside the zeroth-order (specular) lobe. With M held fixed, increasing δ expands the physical aperture and yields narrower angular profiles which can raise the peak levels at certain directions. This apparent gain improvement relative to ideal continuous-phase control, however, is primarily a consequence of the increased aperture size rather than an intrinsic advantage of periodic steering under fixed-footprint constraints.

4) Aperture-matched comparison: Diffraction-order designs can exhibit high target-lobe peaks in the unconstrained setting since selecting a larger period δ increases the physical aperture when M is held fixed. To enable a fair “apples-to-apples” comparison, Fig. 12 evaluates diffraction-order and dense ON/OFF masking under a fixed physical footprint. In this aperture-matched setting, increasing δ reduces the number of active cells or elements that fit within the fixed length and thereby lowers the coherent gain to the desired diffraction order.

As shown in Fig. 12(a), for the single-target case $(\theta_I, \theta_T) = (45^\circ, -10^\circ)$, the dense ON/OFF mask on the $\lambda/2$ maintains a larger effective number of contributing cells and therefore sustains stronger target response than the aperture-matched diffraction-order design. Fig. 12(b) shows the same trend in the multi-target setting where periodic steering becomes less efficient due to a sparser effective aperture. This reduces coherent accumulation at each intended non-specular direction.

The associated sidelobe behavior follows from the underlying aperture structures. In the ON/OFF case, binary amplitude quantization introduces additional spatial harmonics and does

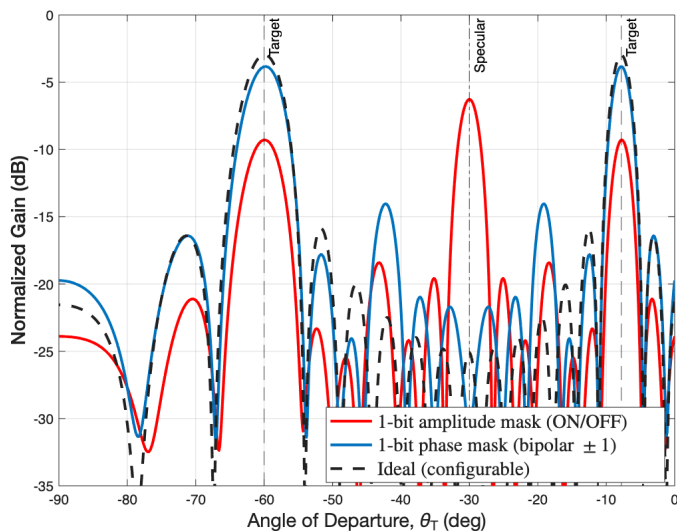


Fig. 10. Theory (60 GHz, $\theta_I = 30^\circ$, $M = 35$): multi-beam synthesis targeting $\theta_T = -7.8^\circ$ and -60° . Normalized gain $\gamma(\theta; \theta_I)$ is shown for the ON/OFF mask, the bipolar (± 1) mask, and the ideal continuous-phase reflector.

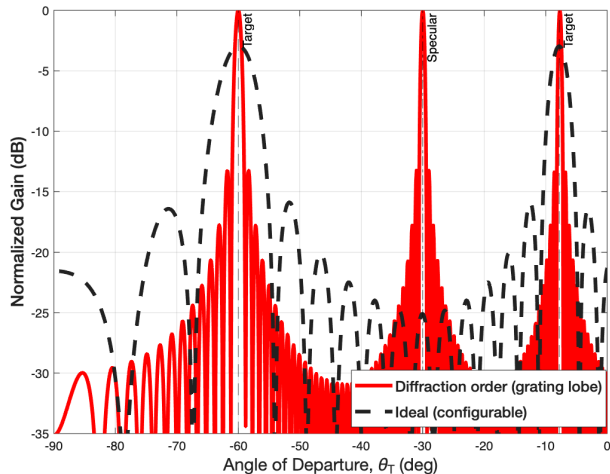


Fig. 11. Theory (60 GHz, $\theta_I = 30^\circ$, $M = 35$): diffraction-order multi-lobe example with $\delta = 13.66$ mm, producing additional visible orders alongside the zeroth-order (specular) response.

not fully suppress the residual specular component, leading to stronger secondary lobes than in the ideal continuous-phase case. In the diffraction-order case, additional lobes are an inherent consequence of the periodic aperture structure, since the desired beam is realized as a selected diffraction order of a passive periodic reflector. Overall, these results indicate that under fixed-size deployment constraints, dense ON/OFF masking is typically preferable because it preserves a larger effective aperture and stronger target-direction gain. By contrast, diffraction-order steering is attractive when aperture expansion is permitted since its synthesis is simple and analytically tractable.

5) *Two-Dimensional Angular Response and Secondary-Lobe Behavior*: To complement the azimuth-plane cuts, Figs. 13–16 show representative 3-D angular patterns and 2-D angular response maps obtained from the planar-aperture model in (4) for both the single-beam and multi-beam cases

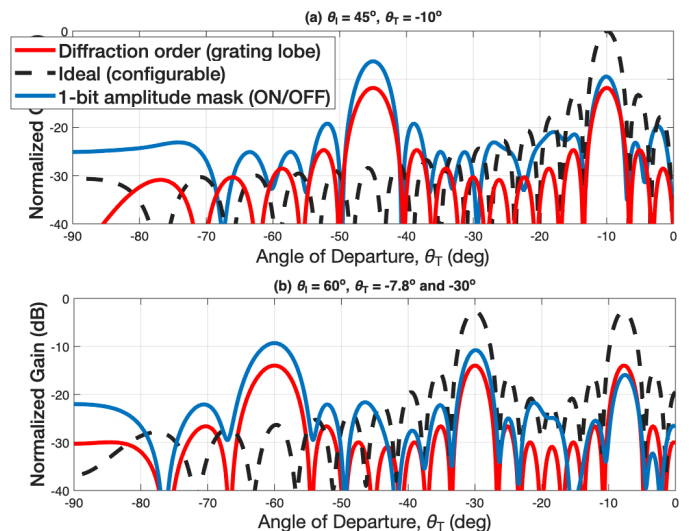


Fig. 12. Theory: aperture-matched comparison of diffraction-order steering and dense ON/OFF masking under fixed physical aperture constraints. (a) Single-target case for $\theta_I = 45^\circ$ and $\theta_T = -10^\circ$. (b) Multi-target case (fixed footprint), illustrating reduced gain for diffraction-order designs when the period increase reduces effective sampling density.

using a 35×35 lattice. These results are consistent with the 1-D azimuthal analysis, while also revealing the response variation with the second angular coordinate ϕ . Since the synthesis in this paper is carried out for azimuth-plane steering, the strongest response remains centered near $\phi = 0$. As $|\phi|$ increases, the response decreases and broadens because the design does not impose independent elevation steering.

For the single-beam case, Figs. 13 and 14 correspond to $\theta_I = 45^\circ$ and $\theta_T = -10^\circ$. The passive all-ON reflector exhibits the expected specular response with dominant energy near $\theta_{\text{spec}} = -45^\circ$. The ideal fixed-phase reflector concentrates energy near the desired target direction. The proposed ON/OFF design also forms a deterministic non-specular lobe toward $\theta_T = -10^\circ$, but with broader secondary structure due to binary quantization and residual specular leakage. The diffraction-order reflector likewise produces a lobe near the target direction, but its periodic structure leads to more pronounced secondary lobes.

For the multi-beam case, Figs. 15 and 16 correspond to $\theta_I = 30^\circ$ with target directions $\theta_T \in \{-7.8^\circ, -60^\circ\}$. The passive all-ON reflector again remains predominantly specular, whereas the ideal fixed-phase reflector produces two intended lobes near the desired target directions. The ON/OFF reflector also enhances both target directions, confirming that deterministic multi-beam shaping can be approximated with a fully passive binary aperture. The diffraction-order reflector shown in these figures is a single-target periodic reference and therefore does not realize both target beams simultaneously. Overall, the 2-D aperture results reinforce the same main conclusion as the 1-D analysis. Fully passive binary-coded apertures can realize deterministic non-specular beam shaping on a fixed dense lattice, while diffraction-order steering offers simpler periodic synthesis at the cost of stronger secondary lobes and reduced flexibility for multi-beam operation.

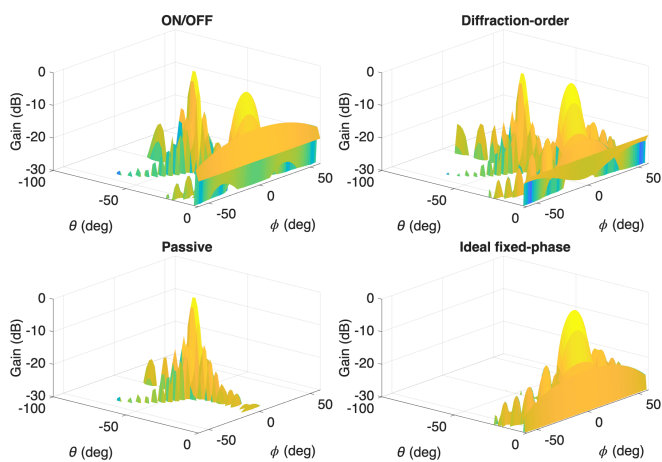


Fig. 13. Three-dimensional angular response patterns at 60 GHz for the representative single-beam case $\theta_I = 45^\circ$ and target $\theta_T = -10^\circ$. The responses are normalized to the peak of each design at 60 GHz.

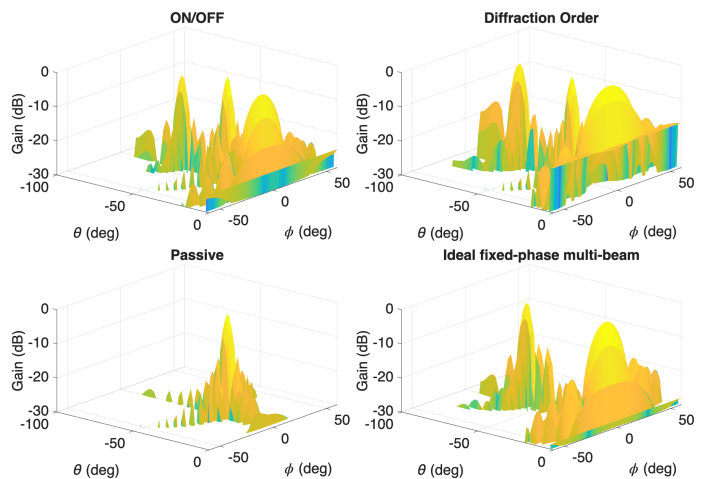


Fig. 15. Three-dimensional angular response patterns at 60 GHz for the representative multi-beam case $\theta_I = 30^\circ$ with target directions $\theta_T \in \{-7.8^\circ, -60^\circ\}$.

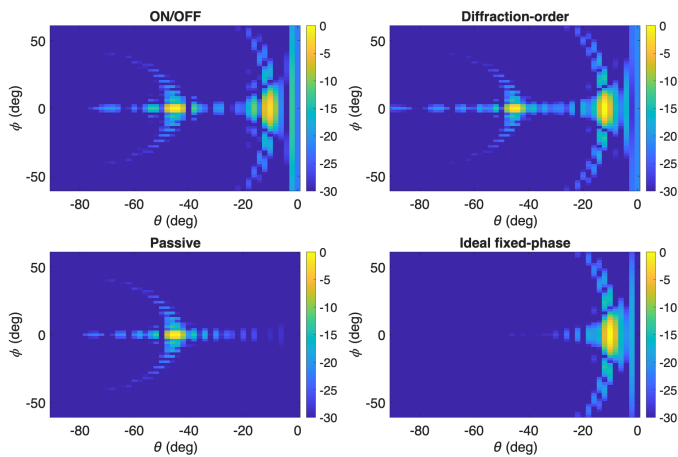


Fig. 14. Two-dimensional angular response maps at 60 GHz for the representative single-beam case $\theta_I = 45^\circ$ and target $\theta_T = -10^\circ$. The plots show the normalized response of the proposed ON/OFF reflector, the diffraction-order reflector, the passive all-ON reflector, and the ideal fixed-phase reflector, evaluated using the 2-D aperture model.

6) *Wideband Sensitivity of Fixed Passive Designs:* Figs. 17 and 18 quantify the wideband sensitivity of the passive designs for the single-beam and multi-beam cases. In both cases, the responses are normalized to the corresponding 60 GHz design-point value so that the off-design loss can be observed directly as the carrier frequency is varied while the physical reflector geometry is held fixed.

For the single-beam case in Fig. 17, all designs exhibit reduced target-direction response as the operating frequency moves away from the design point. The ON/OFF reflector shows a more gradual reduction in target-direction response than the diffraction-order design. This behavior is expected because diffraction-order steering depends explicitly on the ratio between the fixed spatial period and the wavelength, so the selected diffraction order shifts more rapidly as frequency changes. By contrast, the dense ON/OFF aperture is comparatively more tolerant to moderate off-design operation, although it also experiences loss away from the design frequency.

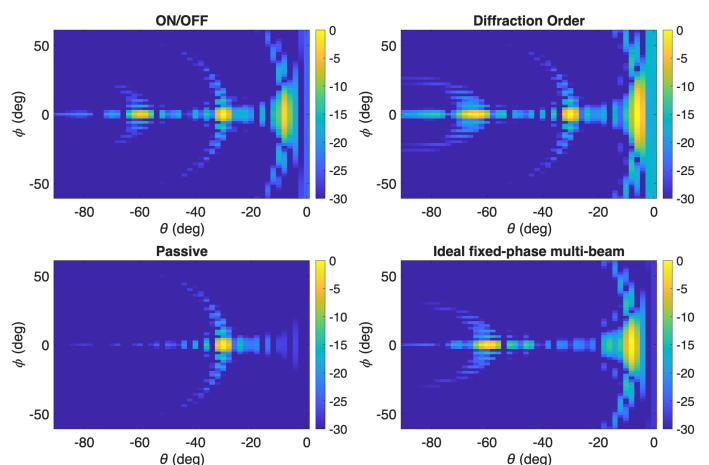


Fig. 16. Two-dimensional angular response maps at 60 GHz for the representative multi-beam case $\theta_I = 30^\circ$ with target directions $\theta_T \in \{-7.8^\circ, -60^\circ\}$. The plots show the normalized response of the proposed ON/OFF reflector, a diffraction-order reflector, the passive all-ON reflector, and the ideal fixed-phase multi-beam reflector, evaluated using the 2-D aperture model.

A similar trend is observed in the multi-beam case shown in Fig. 18. The results again show that fixed passive beam patterns are frequency-sensitive, with the diffraction-order design exhibiting stronger degradation away from the 60 GHz design point. Although the ON/OFF reflector is not frequency-invariant, it maintains more stable target-direction behavior over moderate frequency variation and therefore provides a more robust passive alternative under fixed-aperture operation.

7) *Energy-efficiency implication under surface-power overhead:* Fig. 19 illustrates the impact of surface-side (reflector) operational power on energy efficiency at the target direction $\theta_T = -10^\circ$. Using the definitions in Section VII-B, we evaluate EE under a fixed radio-side power budget $P_0 \triangleq P_{\text{TX}} + P_{\text{circ}}$ and vary only the surface-side term P_{surf} . The achievable rate is obtained from the target-direction SNR using (37). The example parameters used to generate the curves are given in the figure caption. For each reflector design, the target-

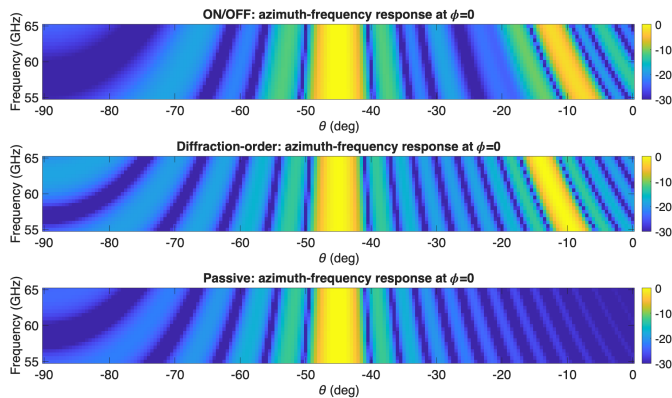


Fig. 17. Target-direction gain variation versus frequency for the single-beam case $\theta_I = 45^\circ$ and $\theta_T = -10^\circ$, normalized to the corresponding 60 GHz response of each design.

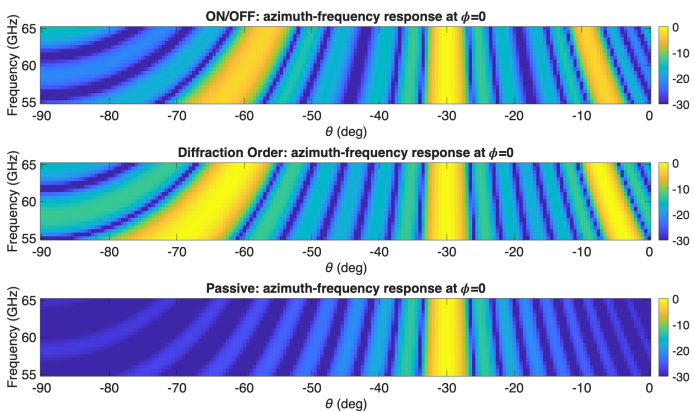


Fig. 18. Target-direction gain variation versus frequency for the multi-beam case $\theta_I = 30^\circ$ with target directions $\theta_T = -7.8^\circ$ and $\theta_T = -60^\circ$, normalized to the corresponding 60 GHz response of each design.

direction $\text{SNR}(\theta_T)$ is scaled according to its relative target gain, so that the resulting curves capture the joint effect of reflector-induced SNR improvement and added surface-side power.

Since the proposed reflectors are fully passive, $P_{\text{surf}} = 0$ and their EE curves remain essentially constant. In contrast, powered RIS baselines exhibit a monotonic EE reduction as P_{surf} increases, because controller/driver overhead and state-dependent unit-cell power increase the denominator of (38) without providing a commensurate increase in $R(\theta_T)$. This behavior is consistent with measurement-backed RIS power decompositions in which the controller term alone can be several watts (e.g., $P_{\text{ctrl}} \approx 4.8$ W [11], [12]). Overall, Fig. 19 highlights that eliminating surface-side operational power allows target-direction beam gains to translate more directly into higher bits/Joule, which is particularly relevant for static indoor installations.

B. Experimental Setup and Results

1) *Experimental setup and processing*: Over the air measurements are performed using a narrowband continuous-wave (CW) excitation at 60.48 GHz, which serves as the design frequency for the fabricated reflectors shown in Fig. 7. Two

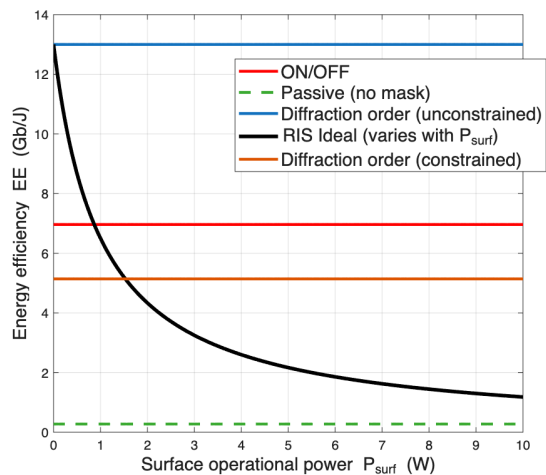


Fig. 19. Energy efficiency $\text{EE} = R/(P_0 + P_{\text{surf}})$ versus surface operational power P_{surf} at $\theta_T = -10^\circ$ for an example setting with $P_0 = 1$ W, $B = 2$ GHz, and baseline $\text{SNR}_0 = -10$ dB. Fully passive designs have $P_{\text{surf}} = 0$ and therefore yield constant EE, whereas a powered RIS baseline decreases with P_{surf} . For the diffraction-order curve, unconstrained indicates that the selected period is applied while allowing the physical aperture to expand.

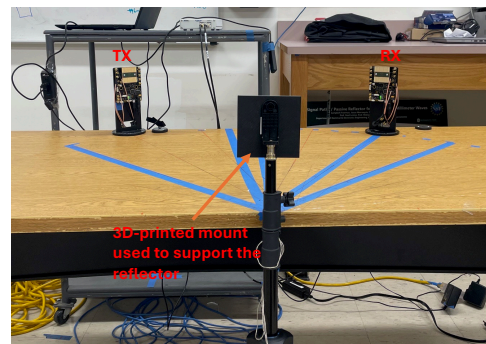


Fig. 20. Over the air azimuthal sweep measurement setup. The transmitter (TX) is fixed at the prescribed incidence angle, while the receiver (RX) is swept in azimuth to measure the scattered response.

Sivers EVK02001 transceiver kits are positioned on a constant-radius arc (0.9 m) centered on the reflector. The transmitter is fixed at azimuth AoA θ_I , while the receiver is swept in azimuth to measure the scattered response versus AoD θ_T . Two reference scans are collected, mount-only (background) and all-ON (reference reflector). Background-subtracted power is computed as

$$P_{\text{bgs}}(\theta_T, \theta_I) = \max\{P_{\text{meas}}(\theta_T, \theta_I) - P_{\text{mount}}(\theta_T, \theta_I), 0\},$$

and target-direction results are reported using

$$G_{\text{norm}}(\theta_T) = 10 \log_{10} \left(\frac{P_{\text{bgs}}(\theta_T)}{\max_{\theta} P_{\text{bgs,all-on}}(\theta)} \right).$$

Since the experimental measurements use a narrowband CW signal, they validate passive beam shaping at the design frequency rather than broadband communication performance.

2) *Experimental Results and Discussion*: We experimentally evaluate the performance of the proposed passive reflector designs for both single-beam and multi-beam scenarios. The single-beam configuration considers an incidence angle of $\theta_I = 45^\circ$ with a target direction $\theta_T = -10^\circ$, while

TABLE II

BACKGROUND-SUBTRACTED (MOUNT-ONLY) RELATIVE RECEIVED POWER FOR THE 3D-PRINTED INKWELL REFLECTORS IN FIG. 7 ($M = 35$ CELLS PER SIDE ON THE BASE SCAFFOLD PRIOR TO METALLIZATION; AZIMUTH SCAN AT FIXED ELEVATION).

AoA	AoD	Scheme	$P_{\text{bgs}}(\theta)$ (dB)	$\Delta P_{\text{bgs}}(\theta)$ (dB)	$G_{\text{norm}}(\theta)$ (dB)
45°	-45°	Passive (all-ON; specular)	-73.05	0.00	0.00
		Metal plate (baseline)	-72.93	+0.12	+0.12
		Proposed ON/OFF (1-bit amplitude)	-77.10	-4.05	-4.05
		Diffraction-order (grating-lobe)	-78.95	-5.90	-5.90
45°	-10°	Passive (all-ON; specular)	-96.57	0.00	-23.52
		Metal plate (baseline)	-95.67	+0.90	-22.62
		Proposed ON/OFF (1-bit amplitude)	-77.29	+19.27	-4.24
		Diffraction-order (grating-lobe)	-78.88	+17.69	-5.83
30°	-7.8°	Passive (all-ON; specular)	-96.48	0.00	-23.43
		Metal plate (baseline)	-92.71	+3.77	-19.66
		Proposed ON/OFF (1-bit amplitude)	-78.70	+17.77	-5.65
		Diffraction-order (grating-lobe)	-79.79	+16.69	-6.74
30°	-60°	Passive (all-ON; specular)	-98.74	0.00	-25.69
		Metal plate (baseline)	-94.57	+4.16	-21.52
		Proposed ON/OFF (1-bit amplitude)	-79.18	+19.56	-6.13
		Diffraction-order (grating-lobe)	-81.41	+17.33	-8.36
30°	-30°	Passive (all-ON; specular)	-73.05	0.00	0.00
		Metal plate (baseline)	-72.89	+0.12	+0.12
		Proposed ON/OFF (1-bit amplitude)	-81.71	-8.66	-8.66
		Diffraction-order (grating-lobe)	-85.77	-12.72	-12.72

the multi-beam case uses $\theta_I = 30^\circ$ with target directions $\theta_T \in \{-7.8^\circ, -60^\circ\}$. In addition to the fabricated all-ON inkwell reflector, a smooth copper plate is included as a reference baseline to verify that the all-ON metallization achieves comparable specular reflection and to establish a consistent conductor benchmark for subsequent comparisons.

Table II reports the background-subtracted response $P_{\text{bgs}}(\theta)$, the enhancement over the passive all-ON baseline $\Delta P_{\text{bgs}}(\theta)$, and the normalized gain $G_{\text{norm}}(\theta)$. The metric $G_{\text{norm}}(\theta)$ measures the target-direction level relative to the maximum background-subtracted response of the passive all-ON scan (specular lobe), and thus indicates how far a given angle lies below the strongest all-ON direction. In contrast, $\Delta P_{\text{bgs}}(\theta) = P_{\text{bgs,design}}(\theta) - P_{\text{bgs,all-ON}}(\theta)$ directly quantifies the gain improvement achieved by a given design over the passive all-ON reflector at the same (θ_I, θ) .

The measurements confirm that the fabricated all-ON reflector behaves similarly to a solid conductor. At the specular directions, the copper-plate and all-ON responses are nearly identical, with only a small difference (about 0.1 dB), indicating that the inkwell metallization with the copper backing provides a high-reflectivity baseline prior to applying any ON/OFF mask. Consistent with specular-dominated scattering under uniform weighting, the passive all-ON response is weak at non-specular targets. For $\theta_I = 45^\circ$, the -10° direction is more than 20 dB below the all-ON peak in terms of $G_{\text{norm}}(\theta)$, demonstrating that an unshaped passive surface does not effectively redirect energy.

Applying ON/OFF masking and diffraction-order synthesis redistributes energy away from the specular direction and toward the intended targets. This redistribution is visible as reduced specular response (negative ΔP_{bgs} at the specular angle) together with large positive enhancement at target

angles. For the single-beam case $(\theta_I, \theta_T) = (45^\circ, -10^\circ)$, the ON/OFF reflector provides a strong target enhancement ($\Delta P_{\text{bgs}} \approx +19$ dB) and the diffraction-order design provides a comparable but slightly smaller improvement ($\approx +18$ dB) under the fixed-footprint constraint. These trends are consistent with the theoretical aperture-matched plots in Fig. 12, where dense ON/OFF masking is favored when the physical aperture is fixed. At the specular angle, both ON/OFF and diffraction-order incur a penalty relative to all-ON because the designs intentionally suppress or reweight a portion of the aperture. For ON/OFF this is fundamentally tied to thinning (approximately 50% activation ratio as shown in Lemma 1).

For the multi-beam case ($\theta_I = 30^\circ$), the ON/OFF and diffraction-order designs produce substantial enhancement at both target angles ($\theta_T = -7.8^\circ$ and -60°), confirming successful deterministic non-specular beam formation in a fully passive implementation. At the specular direction ($\theta_T = -30^\circ$), both designs exhibit reduced response relative to all-ON, which is expected since energy is redirected toward the non-specular targets. We note here that the measured magnitude of these specular losses and target gains do not always match the worst-case theoretical bounds relative to an ideal continuous-phase surface, however, the experimentally relevant comparison is against the passive all-ON baseline, for which the measured target enhancements are consistently large. This is because the theory in Section VIII-A is developed using a 1-D azimuthal array-factor abstraction, whereas the fabricated reflector is a 2-D 35×35 lattice and the measurements are azimuth cuts of a 2-D scattering pattern. Additional aperture extent in the orthogonal dimension, elevation-dependent weighting, and indoor multipath can affect absolute levels and partially explain deviations from idealized 1-D

TABLE III
MEASURED RESPONSE LOSS VERSUS FREQUENCY FOR REPRESENTATIVE ON/OFF AND DIFFRACTION-ORDER REFLECTORS, NORMALIZED TO THE 60.48 GHz DESIGN POINT, FOR $\theta_I = 45^\circ$ AND $\theta_T = -10^\circ$.

Frequency (GHz)	ON/OFF loss (dB)	Diffraction-order loss (dB)
58.32	-1.2	-3.3
60.48	0.0	0.0
62.64	-3.0	-5.4
64.80	-8.0	-11.5
66.90	-14.2	-16.3
69.10	-13.4	-20.7

predictions. Nevertheless, the measured ranking and trends across all-ON, ON/OFF, and diffraction order designs remain consistent with theory.

To experimentally assess frequency sensitivity beyond the nominal 60.48 GHz design point, additional narrowband CW measurements were conducted at 58.32, 60.48, 62.64, 64.80, 66.90, and 69.10 GHz for representative ON/OFF and diffraction-order reflectors in the beam-shaping configuration $\theta_I = 45^\circ$ and $\theta_T = -10^\circ$. The measured responses were normalized to the 60.48 GHz result, and the corresponding losses are summarized in Table III. The results show that the target-direction response at $\theta_T = -10^\circ$ degrades for both reflector types as the operating frequency shifts away from the design frequency. Across all measured frequencies, the diffraction-order reflector consistently exhibits larger loss than the ON/OFF design. For example, at 64.80 GHz the ON/OFF reflector experiences a loss of -8.0 dB compared to -11.5 dB for the diffraction-order design, while at 69.10 GHz the losses increase to -13.4 dB and -20.7 dB, respectively. This behavior is in close agreement with the analytical trends in Fig. 17, confirming that the ON/OFF design is comparatively more robust to frequency variation. This degradation can be understood in terms of the wavelength dependence of the underlying beamforming mechanisms. Diffraction-order steering relies explicitly on the ratio between the fixed spatial period and the wavelength (see (31)), such that changes in frequency shift the effective diffraction condition and reduce gain in the intended direction. In contrast, the ON/OFF design relies on dense spatial modulation of the aperture and is therefore less sensitive to moderate changes in wavelength, although it still experiences performance degradation away from the design point.

IX. CONCLUSION

This paper presented a theory-to-hardware framework for fully passive millimeter-wave beam shaping using in-lab fabricated, low-cost 3D-printed reflectors. Beam patterns are fabrication-coded on a fixed dense lattice using binary masks or periodic activation and realized via stencil-assisted conductive deposition on a copper-backed “inkwell” substrate. Two complementary passive mechanisms were developed and validated: fixed-aperture 1-bit ON/OFF spatial masking for non-specular steering and multi-beam synthesis, and diffraction-order (grating-lobe) steering via uniform period selection to place a chosen diffraction order at a desired departure angle.

The experimental results highlight an important tradeoff between these mechanisms. Diffraction-order steering is attractive due to its simplicity, but it typically produces narrower angular features and is therefore more sensitive to alignment errors and geometric mismatch. It is also more susceptible to beam squint under wideband operation because the grating condition is wavelength dependent. This reduces coherence at a fixed target direction as frequency or angle deviates from the design point. In contrast, dense ON/OFF masking operates on a fixed footprint and provides greater flexibility for shaping the angular response (including multi-beam patterns), with improved robustness to practical deployment tolerances.

Future work will extend the framework to full two-dimensional aperture synthesis for joint azimuth–elevation beam control and polarization engineering, and will investigate semi-static control mechanisms (e.g., swappable masks or mechanically indexed patterns) suitable for indoor millimeter-wave electromagnetic environment shaping. We will also study pattern improvements through fabrication and material optimization, including the impact of cell width (effective metallized aperture per cell), metallization thickness/uniformity, and deposition methods to reduce ohmic loss and improve coherent reradiation efficiency.

APPENDIX A

PROOF OF LEMMA 1: ASYMPTOTIC 50% ACTIVATION RATIO OF THE COSINE-THRESHOLD MASK

Recall that the element locations are $x_m = \left(m - \frac{M-1}{2}\right)d_0$, and define the phase associated with the m th element as

$$\phi_m \triangleq kx_m(\sin \theta_T + \sin \theta_I), \quad k = \frac{2\pi}{\lambda}.$$

Substituting x_m into ϕ_m yields the affine phase progression

$$\begin{aligned} \phi_m &= k\left(m - \frac{M-1}{2}\right)d_0(\sin \theta_T + \sin \theta_I) \\ &= \Delta m + \beta_M, \end{aligned} \quad (39)$$

where $\Delta \triangleq kd_0(\sin \theta_T + \sin \theta_I)$, $\beta_M \triangleq -\Delta \frac{M-1}{2}$. Hence, the phase increment is constant and satisfies $\phi_{m+1} - \phi_m = \Delta$. The cosine-threshold activation rule is given by

$$b_m = \mathbf{1}\{\cos(\phi_m) \geq 0\}.$$

Since $\cos(\cdot)$ is 2π -periodic, the activation depends only on $\phi_m \bmod 2\pi$. Introduce the normalized phase variable

$$u_m \triangleq \frac{\phi_m}{2\pi} \bmod 1 = \left(\frac{\Delta}{2\pi}m + \frac{\beta_M}{2\pi}\right) \bmod 1.$$

Under the condition $\Delta/(2\pi) \notin \mathbb{Q}$ (equivalently $\Delta/\pi \notin \mathbb{Q}$), the sequence $\{u_m\}_{m \geq 0}$ is uniformly distributed on $[0, 1)$ by Weyl’s equidistribution theorem. Equivalently, $\phi_m \bmod 2\pi$ is uniformly distributed on the unit circle, with u_m providing a convenient normalized representation. To relate equidistribution to the cosine-threshold activation rule, define the function

$$f(u) \triangleq \mathbf{1}\{\cos(2\pi u) \geq 0\}.$$

This choice of f directly encodes the ON/OFF masking rule in normalized phase coordinates, since

$$b_m = \mathbf{1}\{\cos(\phi_m) \geq 0\} = \mathbf{1}\{\cos(2\pi u_m) \geq 0\} = f(u_m).$$

By the defining consequence of equidistribution, for any Riemann-integrable function $f : [0, 1) \rightarrow \mathbb{R}$,

$$\frac{1}{M} \sum_{m=0}^{M-1} f(u_m) \xrightarrow{M \rightarrow \infty} \int_0^1 f(u) du.$$

Applying this result to the above choice of $f(u)$ yields

$$\begin{aligned} \eta_M &= \frac{1}{M} \sum_{m=0}^{M-1} \mathbf{1}\{\cos(\phi_m) \geq 0\} \\ &= \frac{1}{M} \sum_{m=0}^{M-1} f(u_m) \xrightarrow{M \rightarrow \infty} \int_0^1 \mathbf{1}\{\cos(2\pi u) \geq 0\} du. \end{aligned} \quad (40)$$

The limiting integral corresponds to the fraction of the unit interval for which the cosine-threshold condition is satisfied. Define the set

$$\mathcal{S}_+ \triangleq \{u \in [0, 1) : \cos(2\pi u) \geq 0\} = \left[0, \frac{1}{4}\right] \cup \left[\frac{3}{4}, 1\right).$$

Since the integral of an indicator function equals the Lebesgue measure of its support, we obtain

$$\int_0^1 \mathbf{1}\{\cos(2\pi u) \geq 0\} du = |\mathcal{S}_+| = \frac{1}{2}.$$

Therefore,

$$\eta_M \xrightarrow{M \rightarrow \infty} \frac{1}{2}.$$

This establishes the asymptotic 50% activation ratio and completes the proof of Lemma 1.

APPENDIX B PROOF OF LEMMA 2

Consider a complex number z , its magnitude can be written as $|z| = \max_{\varphi \in [0, 2\pi)} \Re\{e^{-j\varphi} z\}$. Applying this to S_M^* in (23) and exchanging the two maximizations gives

$$\begin{aligned} S_M^* &= \max_{\mathbf{b} \in \{0,1\}^M} \max_{\varphi \in [0, 2\pi)} \Re\left\{e^{-j\varphi} \sum_{m=0}^{M-1} b_m e^{-j\phi_m}\right\} \\ &= \max_{\varphi \in [0, 2\pi)} \max_{\mathbf{b} \in \{0,1\}^M} \sum_{m=0}^{M-1} b_m \cos(\phi_m + \varphi). \end{aligned} \quad (41)$$

For fixed φ , the inner maximization is separable in m and, since $b_m \in \{0, 1\}$, we have $\max_{b_m \in \{0,1\}} b_m \cos(\phi_m + \varphi) = [\cos(\phi_m + \varphi)]_+$, where $[x]_+ \triangleq \max\{x, 0\}$. Define the normalized objective $F_M(\varphi) \triangleq \frac{1}{M} \sum_{m=0}^{M-1} [\cos(\phi_m + \varphi)]_+$, so that (41) can be written compactly as

$$\frac{S_M^*}{M} = \max_{\varphi \in [0, 2\pi)} F_M(\varphi). \quad (42)$$

A distribution-free lower bound can be obtained by noting that the maximum of a function is no smaller than its average, hence

$$\max_{\varphi} F_M(\varphi) \geq \frac{1}{2\pi} \int_0^{2\pi} F_M(\varphi) d\varphi. \quad (43)$$

Interchanging the finite sum and the integral (by linearity) and then applying the change of variables $u = \phi_m + \varphi$ gives

$$\begin{aligned} \frac{1}{2\pi} \int_0^{2\pi} F_M(\varphi) d\varphi &= \frac{1}{M} \sum_{m=0}^{M-1} \frac{1}{2\pi} \int_0^{2\pi} [\cos(\phi_m + \varphi)]_+ d\varphi \\ &= \frac{1}{2\pi} \int_0^{2\pi} [\cos u]_+ du, \end{aligned} \quad (44)$$

where the first equality follows from linearity and the change of variables $u = \phi_m + \varphi$ is used in the second step. Since $[\cos(\cdot)]_+$ is 2π -periodic, each term in the sum is identical and independent of m . Averaging therefore removes element-dependent phase offsets. Note the integrand $[\cos u]_+$ equals $\cos u$ on $u \in [-\frac{\pi}{2}, \frac{\pi}{2}] \pmod{2\pi}$ and is zero elsewhere; therefore $\int_0^{2\pi} [\cos u]_+ du = \int_{-\pi/2}^{\pi/2} \cos u du = 2$. Combining with (44) yields $\frac{1}{2\pi} \int_0^{2\pi} F_M(\varphi) d\varphi = \frac{1}{\pi}$. Using (42) and (43) we conclude

$$\frac{S_M^*}{M} = \max_{\varphi} F_M(\varphi) \geq \frac{1}{\pi},$$

which proves the amplitude bound (25). Squaring both sides yields $\gamma^* \geq 1/\pi^2$, completing the proof.

REFERENCES

- [1] C.-X. Wang *et al.*, "On the road to 6G: Visions, requirements, key technologies and testbeds," *IEEE Commun. Surveys Tuts.*, vol. 25, no. 2, pp. 905–974, Feb. 2023.
- [2] Q. Xue *et al.*, "A survey of beam management for mmWave and THz communications towards 6G," *IEEE Commun. Surveys Tuts.*, vol. 26, no. 3, pp. 1520–1559, 3rd Quart. 2024.
- [3] M. Ahmed *et al.*, "A survey on RIS advances in terahertz communications: Emerging paradigms and research frontiers," *IEEE Access*, vol. 12, pp. 173867–173901, 2024.
- [4] Y. Xing and T. S. Rappaport, "Millimeter wave and sub-terahertz spatial statistical channel modeling for wireless communications," *IEEE J. Sel. Areas Commun.*, vol. 39, no. 6, pp. 1506–1524, Jun. 2021.
- [5] R. W. Heath *et al.*, "An overview of signal processing techniques for millimeter wave MIMO systems," *IEEE J. Sel. Topics Signal Process.*, vol. 10, no. 3, pp. 436–453, Apr. 2016.
- [6] A. Taha, M. Alrabeiah, and A. Alkhateeb, "Enabling large intelligent surfaces with compressive sensing and deep learning," *IEEE Access*, vol. 9, pp. 44304–44321, 2021.
- [7] C. Huang, A. Zappone, G. C. Alexandropoulos, M. Debbah, and C. Yuen, "Reconfigurable intelligent surfaces for energy efficiency in wireless communication," *IEEE Trans. Wireless Commun.*, vol. 18, no. 8, pp. 4157–4170, Aug. 2019.
- [8] M. A. ElMossallamy *et al.*, "Reconfigurable intelligent surfaces for wireless communications: Principles, challenges, and opportunities," *IEEE Trans. Cogn. Commun. Netw.*, vol. 6, no. 3, pp. 990–1012, Sep. 2020.
- [9] S. V. Hum and J. Perruisseau-Carrier, "Reconfigurable reflectarrays and array lenses for dynamic antenna beam control: A review," *IEEE Trans. Antennas Propag.*, vol. 62, no. 1, pp. 183–198, Jan. 2014.
- [10] Y. Liu *et al.*, "Reconfigurable intelligent surfaces: Principles and opportunities," *IEEE Commun. Surveys Tuts.*, vol. 23, no. 3, pp. 1546–1577, 3rd Quart. 2021.
- [11] J. Wang, W. Tang, S. Jin, X. Li, and M. Matthaiou, "Static power consumption modeling and measurement of reconfigurable intelligent surfaces," in *Proc. 31st Eur. Signal Process. Conf. (EUSIPCO)*, 2023, pp. 890–894.
- [12] J. Wang, W. Tang, J. C. Liang, L. Zhang, J. Y. Dai, X. Li, S. Jin, Q. Cheng, and T. J. Cui, "Reconfigurable intelligent surface: Power consumption modeling and practical measurement validation," *IEEE Trans. Commun.*, vol. 72, no. 9, pp. 5720–5734, Sep. 2024.
- [13] J.-B. Gros, V. Popov, M. A. Odit, V. Lenets, and G. Lerosey, "A reconfigurable intelligent surface at mmWave based on a binary phase tunable metasurface," *IEEE Open J. Commun. Soc.*, vol. 2, pp. 1055–1064, 2021.

- [14] H. Kamoda, T. Iwasaki, J. Tsumochi, T. Kuki, and O. Hashimoto, "60-GHz electronically reconfigurable large reflectarray using single-bit phase shifters," *IEEE Trans. Antennas Propag.*, vol. 59, no. 7, pp. 2524–2531, Jul. 2011.
- [15] A. S. Shekhawat, B. G. Kashyap, R. W. Raldiris Torres, F. Shan, and G. C. Trichopoulos, "A millimeter-wave single-bit reconfigurable intelligent surface with high-resolution beam-steering and suppressed quantization lobe," *IEEE Open J. Antennas Propag.*, vol. 6, no. 1, pp. 311–325, Feb. 2025.
- [16] A. H. Naqvi, D. A. Pham, S. I. H. Shah, and S. Lim, "1-bit transmission-type digital programmable coding metasurface with multi-functional beam-shaping capability for Ka-band applications," *Micromachines*, vol. 14, no. 6, Art. no. 1250, Jun. 2023.
- [17] T. Huang, W. Fu, D. Lu, Y. Pan, M. Wang, and Y. Yan, "Wideband 1-bit reconfigurable transmission metasurface unit cell design in Ka-band with polarization hold and conversion," *Scientific Reports*, vol. 13, Art. no. 20076, Nov. 2023.
- [18] P. Li, T. Yang, J. Ren, and Y. Yin, "Design of 1-bit reconfigurable reflectarray based on miniaturized reconfigurable unit," in *Proc. IEEE Int. Microwave Workshop Series on Antennas and Propagation (IMWS-AMP)*, Chongqing, China, Nov. 2021, pp. 370–372.
- [19] W. Khawaja, O. Ozdemir, Y. Yapici, F. Erden, and I. Guvenc, "Coverage enhancement for NLoS mmWave links using passive reflectors," *IEEE Open J. Commun. Soc.*, vol. 1, pp. 263–281, 2020.
- [20] Z. Peng *et al.*, "An effective coverage scheme with passive-reflectors for urban millimeter-wave communication," *IEEE Antennas Wireless Propag. Lett.*, vol. 15, pp. 398–401, 2016.
- [21] A. P. Ganesh, W. Khawaja, O. Ozdemir, I. Guvenc, H. Nomoto, and Y. Ide, "Propagation measurements and coverage analysis for mmWave and sub-THz frequency bands with transparent reflectors," in *Proc. IEEE 97th Veh. Technol. Conf. (VTC2023-Spring)*, Jun. 2023, pp. 1–6.
- [22] O. Ibrahim, R. S. S. Bandari, and M. E. Eltayeb, "LiDAR-aided millimeter-wave range extension using a passive mirror reflector," in *Proc. IEEE 22nd Consum. Commun. Netw. Conf. (CCNC)*, Jan. 2025, pp. 1–4.
- [23] S. Häger, M. Danger, K. Heimann, Y. Gümüs, S. Böcker, and C. Wietfeld, "Custom design and experimental evaluation of passive reflectors for mmWave private networks," in *Proc. IEEE 30th Int. Symp. Local and Metropolitan Area Netw. (LANMAN)*, Boston, MA, USA, 2024, pp. 52–57.
- [24] K. Qian *et al.*, "MilliMirror: 3D printed reflecting surface for millimeter-wave coverage expansion," in *Proc. 28th Annu. Int. Conf. Mobile Comput. Netw. (MobiCom)*, Oct. 2022, pp. 15–28.
- [25] K. Qian and X. Zhang, "Demo: Fully passive 3D printed reflecting surface for millimeter-wave coverage expansion," in *Proc. 20th Annu. Int. Conf. Mobile Syst., Appl. Serv. (MobiSys)*, Jun. 2022, pp. 1–2.
- [26] H. L. Van Trees, *Optimum Array Processing (Detection, Estimation, and Modulation Theory, Part IV)*. Wiley-Interscience, 2002.
- [27] SilxCore Conductive Paint, product page. [Online]. Available: <https://www.amazon.com/dp/B0DJTYJD7V>
- [28] M. Rihan, A. Zappone, S. Buzzi, G. Fodor, and M. Debbah, "Passive versus active reconfigurable intelligent surfaces for integrated sensing and communication: Challenges and opportunities," *IEEE Network*, vol. 38, no. 3, pp. 218–226, May 2024.
- [29] Q. Wu and R. Zhang, "Beamforming optimization for wireless network aided by intelligent reflecting surface with discrete phase shifts," *IEEE Trans. Commun.*, vol. 68, no. 3, pp. 1838–1851, Mar. 2020.